Journal of Alloys and Compounds 509 (2011) 656–668

Contents lists available at ScienceDirect

Journal of Alloys and Compounds

journal homepage: www.elsevier.com/locate/jallcom

Microstructures and liquidus projection of the ternary Ag–Sb–Te system

Hsin-jay Wu, Sinn-wen Chen*

Department of Chemical Engineering, National Tsing Hua University, #101, Sec. 2, Kuang-Fu Road, Hsin-Chu 300, Taiwan

ARTICLE INFO

Article history:
Received 17 July 2010
Received in revised form
25 September 2010
Accepted 29 September 2010
Available online 8 October 2010

Keywords:
Solidification
Microstructure
Thermoelectric materials

ABSTRACT

Ag–Sb–Te alloys are important for thermoelectric applications. Fifty-one Ag–Sb–Te ternary alloys were prepared, and their primary solidification phases were analyzed. The liquidus troughs of the liquidus projection of the ternary Ag–Sb–Te system are determined based on the experimental results and the phase diagrams of the three binary constituent systems. There are 13 primary solidification phase regions. In addition to the three terminal solid solution phases and nine binary compounds, there is one ternary compound, $AgSbTe_2$. A unique microstructure with bright spherical phases uniformly dispersed in a matrix caused by a miscibility gap in the liquid phase is found in the γ-Ag_2Te primary solidification phase regime. A very fine microstructure with nanometer size Ag_2Te is also observed, resulting from the class I reaction, liquid = δ + Ag_2Te + $AgSbTe_2$, at 496.5 °C, and the liquid composition of Ag–40.0 at%Sb–36.0 at%Te.

1. Introduction

Thermoelectric materials have been intensively investigated recently due to their small size and direct electric–thermal energy conversion in applications [1–7]. As one of the most promising thermoelectric materials [6], $AgSbTe_2$ compound is an important component of many promising thermoelectric materials, such as $AgPb_mSbTe_{2m}$ [3,4] and TAGS-x alloy [7,8]. TAGS-x stands for $AgSbTe_{2(1-x)}GeTe_x$ whose figure-of-merit value ZT is 1.4 at 750 K when x is 85, and 1.7 at 700 K when x is 80. The ZT of the $AgPb_mSbTe_{2m}$ bulk thermoelectric material is as high as 2.2 at 800 K when m is 10 [3]. The $ZT = (S^2\sigma/\kappa)T$ is the most critical property of thermoelectric materials where S is the Seebeck coefficient, σ is the electrical conductivity and κ is the thermal conductivity [1–6].

Although very promising ZT values have been found in Ag–Sb–Te and Ag–Sb–Te-based materials, complicated domains affecting the efficiency of their bulk properties have been reported [9]. Results from previous studies clearly indicate that the thermoelectric properties are strongly influenced by the existing phases and microstructures [10–12], but fundamental understanding of the phase and microstructure formation is lacking. Liquidus projection is the projection of the liquidus troughs of a space phase diagram [13–15], and it is an important type of fundamental material information. Liquidus projection depicts the compositional ranges of different primary solidification phases, the first solidification phases, and it is very useful in the understanding of phase formation during solidification.

This study carries out experimental determination of the liquidus projection of the ternary Ag–Sb–Te system. Various Ag–Sb–Te alloys are prepared. The phase transformation temperatures are determined using DTA (differential thermal analysis). The primary solidification phases of the as-solidified Ag–Sb–Te alloys are metallographically examined. Based on the phase relationships of the constituent binary systems [16–18], the information of the primary solidification phases and thermal analysis results, the Ag–Sb–Te liquidus projection is then constructed. This fundamental information is useful for analyzing the microstructural development and phase formation, and is essential for designing and understanding the Ag–Sb–Te thermoelectric materials.

2. Experimental procedures

Ternary Ag–Sb–Te alloys were prepared with pure Ag shots (99.99 wt%, Aldrich, USA), Sb pellets (99.999 wt%, Sigma–Aldrich, USA), and Te pellets (99.99 wt%, Aldrich, Saint Louis, USA). Proper amounts of constituent elements were weighed and encapsulated in quartz tubes at a pressure of 10^{-5} bar. The total mass of one ingot is about 1 g. The sample capsule was first placed in a furnace at 800 °C for 4 h, and 1000 °C for another 4 h for the alloys at the Ag-rich corner, to ensure complete mixing of the constituent elements. The capsule was then quenched in water.

The quenched alloys were cut into parts. One part was metallographically examined using scanning electron microscopy (SEM, Hitachi, S-2500, Japan), and the phase compositions were determined by energy dispersive X-ray spectroscopy (EDS) and field-emission electron-probe microanalysis (FE-EPMA, JEOL, JXA-8500F, Japan). The phase transformation temperatures were determined by DTA (Perkin Elmer DTA7, USA) with 4 °C/min heating and cooling rates. Powder X-ray diffraction analysis (XRD, Scintac, XDS-2000 V/H, USA) with Cu-Ka as the radiation source was also conducted for phase determination.

* Corresponding author. Tel.: +886 3 5721734; fax: +886 3 5715408.
E-mail address: swchen@mx.nthu.edu.tw (S.-w. Chen).

0925-8388/$ – see front matter © 2010 Elsevier B.V. All rights reserved.
doi:10.1016/j.jallcom.2010.09.200

Table 1
Nominal compositions and primary solidification phase of the ternary Ag–Sb–Te alloys.

No.	Nominal composition (at%)			Primary phase
	Ag	Sb	Te	
1	25.0	5.0	70.0	Te
2	20.0	10.0	70.0	Te
3	10.0	20.0	70.0	Sb_2Te_3
4	15.0	20.0	65.0	Sb_2Te_3
5	20.0	20.0	60.0	Sb_2Te_3
6	10.0	30.0	60.0	Sb_2Te_3
7	11.0	35.0	54.0	Sb_2Te_3
8	5.0	40.0	55.0	Sb_2Te_3
9	10.0	40.0	50.0	γ
10	17.0	45.0	38.0	δ
11	10.0	50.0	40.0	δ
12	14.0	50.0	36.0	δ
13	5.0	55.0	40.0	δ
14	10.0	60.0	30.0	δ
15	25.0	50.0	25.0	Sb
16	15.0	60.0	25.0	Sb
17	20.0	60.0	20.0	Sb
18	90.0	3.0	7.0	Ag
19	90.0	5.0	5.0	Ag
20	85.0	10.0	5.0	Ag
21	30.0	30.0	40.0	γ-Ag_2Te
22	34.0	30.0	36.0	γ-Ag_2Te
23	27.0	35.0	38.0	γ-Ag_2Te
24	24.0	40.0	36.0	–
25	30.0	40.0	30.0	γ-Ag_2Te
26	25.0	45.0	30.0	γ-Ag_2Te
27	20.0	50.0	30.0	γ-Ag_2Te
28	40.0	20.0	40.0	γ-Ag_2Te
29	45.0	20.0	35.0	γ-Ag_2Te
30	60.0	20.0	20.0	γ-Ag_2Te
31	65.0	30.0	5.0	γ-Ag_2Te
32	55.0	10.0	35.0	γ-Ag_2Te
33	75.0	13.0	12.0	ξ
34	70.0	5.0	25.0	ξ
35	77.0	8.0	15.0	ξ
36	82.0	5.0	13.0	Ag
37	50.0	5.0	45.0	β-Ag_2Te
38	52.0	3.0	45.0	β-Ag_2Te
39	43.0	5.0	52.0	β-$Ag_{1.9}Te$
40	39.0	5.0	56.0	β-Ag_5Te_3
41	35.0	5.0	60.0	β-Ag_5Te_3
42	30.0	10.0	60.0	$AgSbTe_2$
43	34.0	10.0	56.0	$AgSbTe_2$
44	38.0	10.0	52.0	$AgSbTe_2$
45	45.0	10.0	45.0	$AgSbTe_2$
46	40.0	15.0	45.0	–
47	28.0	20.0	52.0	$AgSbTe_2$
48	35.0	20.0	45.0	$AgSbTe_2$
49	20.0	30.0	50.0	$AgSbTe_2$
50	20.0	35.0	45.0	$AgSbTe_2$
51	20.0	40.0	40.0	$AgSbTe_2$

3. Results and discussions

Fifty-one Ag–Sb–Te alloys were prepared. Their nominal compositions were calculated based on the mass measurements of the constituent elements used for the sample preparation, and are summarized in Table 1 and shown in Fig. 1(a). Since liquidus trough projection delineates the compositional regimes of primary solidification phases, the boundaries of Ag–Sb–Te liquidus projection are determined from the results of the primary solidification phases which are identified through the as-quenched alloys and the phase diagrams of the three constituent binary systems [16–18]. The temperature descending direction of the liquidus trough lines are determined from the thermal analysis results. The liquidus projection of Ag–Sb–Te has thus been determined as shown in Fig. 1(a) and (b). The metallographic and thermal analysis results are illustrated below.

3.1. Primary phase: Te

Fig. 2(a) is the backscattering electron image (BEI) of alloy#1 (Ag–5.0 at%Sb–70.0 at%Te). Three different phase regions are observed, including the bright dendritic phase, the dark phase formed along the isles of the dendrites and a eutectic microstructure region. Based on the microstructure [19,20], it is concluded that the bright dendritic phase is the primary solidification phase. Its composition is 99.0 at%Te, as determined by EDS, and it is a Te phase with very small Ag and Sb solubilities. Similar results are found for the alloy#2 (Ag–10.0 at%Sb–70.0 at%Te), with the Te phase is its primary solidification phase as well.

In addition to the primary solidification phase, the other phase regions of alloy#1 are also examined. As shown in Fig. 1(a), the solidification path moves away from the Te corner with the precipitation of the Te phase, which intercepts the liquidus trough line, i.e. the Te/Ag_5Te_3 univariant line. The average composition of the fine-microstructure region is Ag–5.0 at%Sb–64.6 at%Te. It is likely

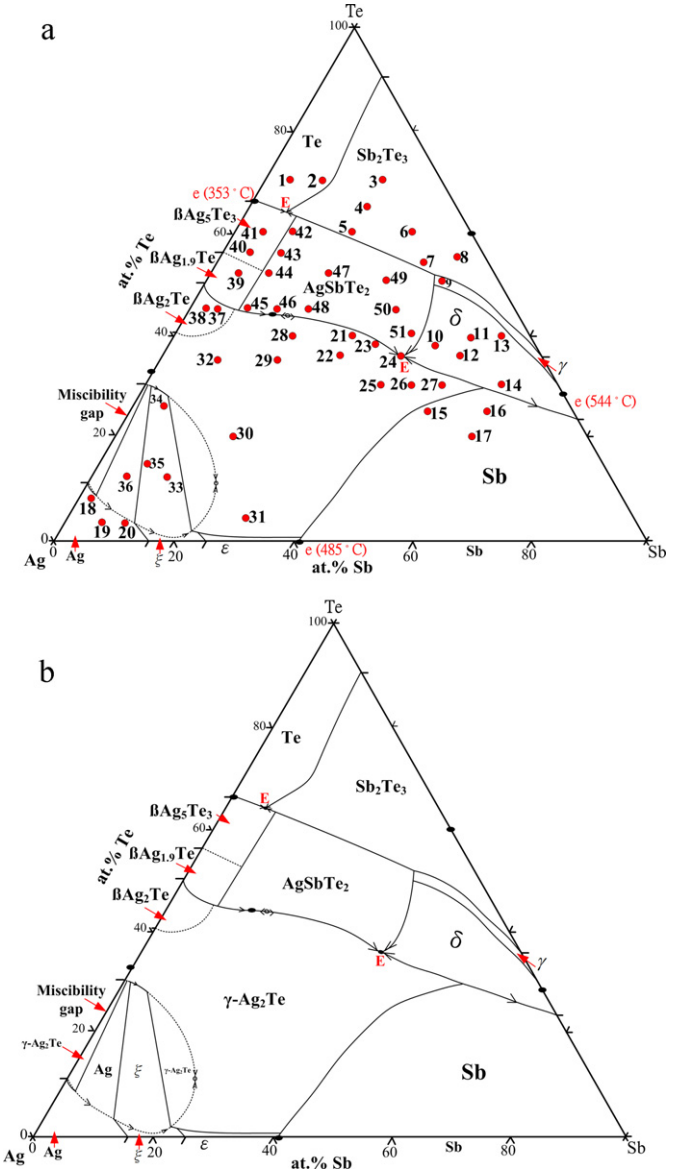

Fig. 1. (a) Liquidus projection of the ternary Ag–Sb–Te system and the nominal compositions of the alloys carried out in this study. (b) Liquidus projection of the ternary Ag–Sb–Te system constructed through experimental results.

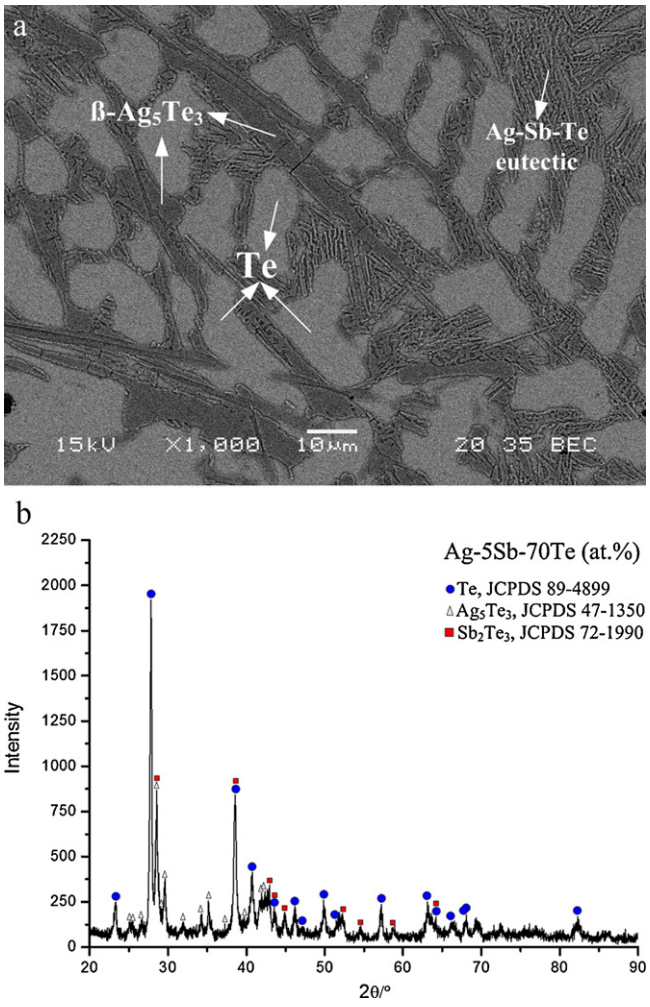

Fig. 2. (a) BEI micrograph of as-solidified alloy#1 (Ag–5.0 at%Sb–70.0 at%Te). (b) X-ray diffraction pattern of as-solidified alloy#1 (Ag–5.0 at%Sb–70.0 at%Te).

the last solidified region, and it goes through the class I reaction, liquid = Te + Sb_2Te_3 + Ag_5Te_3. The XRD results, as shown Fig. 2(b), are consistent with the microstructural analysis.

3.2. Primary phase: Sb_2Te_3

Fig. 3(a) is the BEI micrograph of as-cast alloy#3 (Ag–20.0 at%Sb–70.0 at%Te). The gray dendritic phase is the primary solidification phase. Its composition is Ag–39.8 at%Sb–58.8 at%Te and it is a Sb_2Te_3 phase with l.5 at%Ag solubility. Similar results are found for alloys#4–#8 for which Sb_2Te_3 is also the primary solidification phase. The composition of the bright phase adjacent to the dendritic phase is Sb–96.7 at%Te and is in the Te phase with negligible Ag. As shown in the liquidus projection of Fig. 1(a), the solidification path moves toward the Sb_2Te_3/Te univariant line with the precipitation of the Sb_2Te_3 phase and the Te phase is the secondary solidification phase. Fig. 3(b) is the X-ray diffraction pattern for alloy#3, which clearly illustrates the three solidified phases.

Fig. 3(c) is the BEI micrograph of alloy#5 (Ag–20.0 at%Sb–60.0 at%Te). As mentioned previously, similar to the alloy#3, its primary solidification phase is the Sb_2Te_3 phase. However, the secondary phase is not the bright Te phase as in as-cast alloy#3. A darker phase is formed adjacent to the Sb_2Te_3 phase and between the dendrites. Its composition is Ag–32.7 at%Sb–49.9 at%Te and it is an $AgSbTe_2$ phase. As shown in Fig. 1(a), due to the differences of their nominal compositions, the solidification path of alloy#5 moves toward the Sb_2Te_3/$AgSbTe_2$ univariant line instead of the Sb_2Te_3/Te, as in the case of alloy#3. In addition to these phases, regions with fine structures can also be observed in Fig. 3(a) and (c).

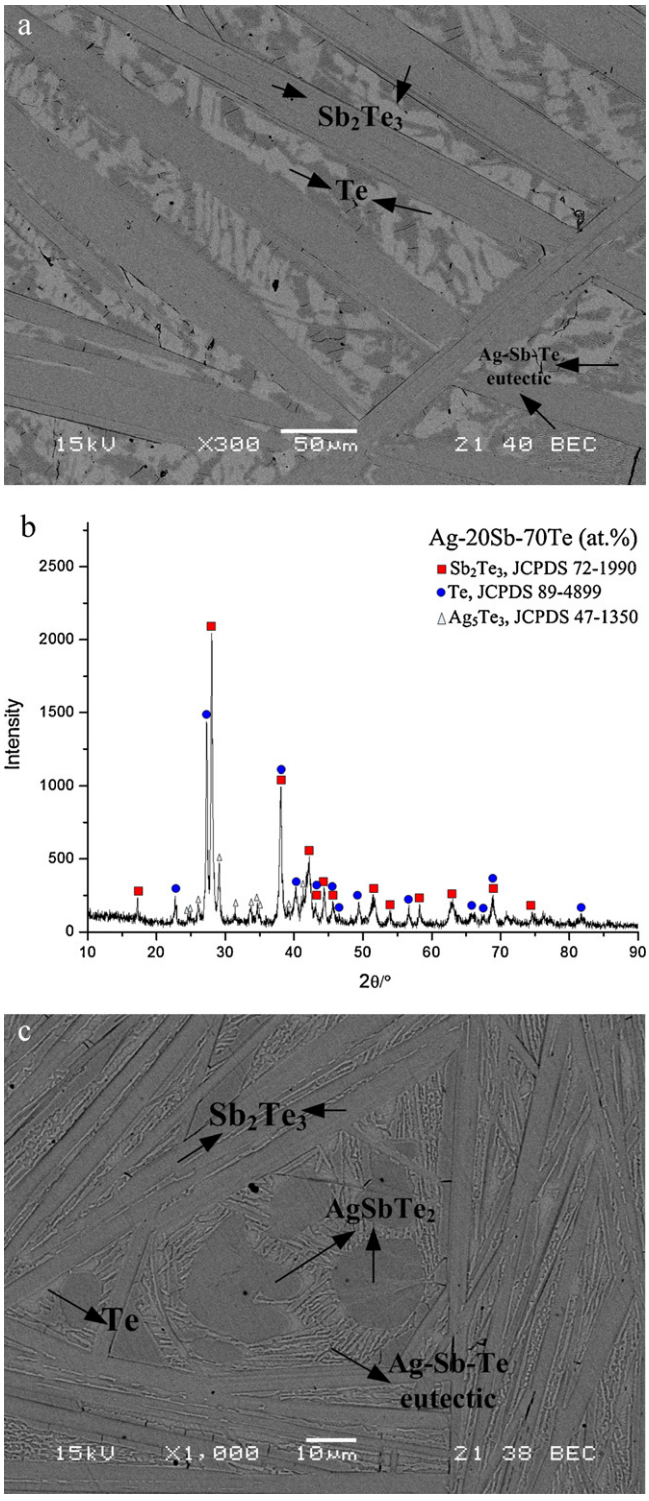

Fig. 3. (a) BEI micrograph of as-solidified alloy#3 (Ag–20.0 at%Sb–70.0 at%Te). (b) X-ray diffraction pattern of as-solidified alloy#3 (Ag–20.0 at%Sb–70.0 at%Te). (c) BEI micrograph of as-solidified alloy#5 (Ag–20.0 at%Sb–60.0 at%Te).

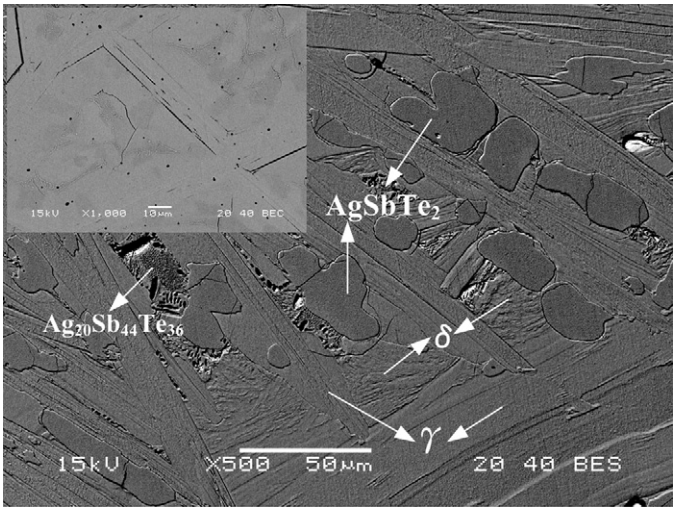

Fig. 4. BEI micrograph of as-solidified alloy#9 (Ag–40.0 at%Sb–50.0 at%Te).

3.3. Primary phase: γ

Fig. 4 is the BEI micrograph of as-cast alloy#9 (Ag–40.0 at%Sb–50.0 at%Te). The composition of the dendritic phase is Ag–41.4 at%Sb–52.3 at%Te, and it is a γ phase with a small amount of Ag solubility. In addition to the primary solidification γ phase, significant amounts of the $AgSbTe_2$ phase and δ phase are observed in as-cast alloy#9. The results clearly indicate that the temperature descending direction of the γ/$AgSbTe_2$ and δ/$AgSbTe_2$ univariant lines move from the Te corner toward the Ag–Sb side, and the $AgSbTe_2$ phase and δ phase solidify after the solidification of the Sb_2Te_3 phase.

3.4. Primary phase: δ

Fig. 5(a) is the BEI of as-cast alloy#14 (Ag–60.0 at%Sb–30.0 at%Te). The average composition of the primary solidification phase is Ag–62.9 at%Sb–32.6 at%Te, which is in the δ phase with 4.6% solubility of Ag. In addition to the δ phase, the Ag_2Te phase and regions of eutectic structure are observed. With the precipitation of the δ phase, the residual liquid moves toward the δ/Ag_2Te univariant line. The average composition of the fine structure region is Ag–44.0 at%Sb–36.0 at%Te, which is likely the last solidified region through the liquid = δ + Ag_2Te + $AgSbTe_2$ class I reaction. Similar results are found for alloys#10–#13, and the primary solidification phase is the δ phase. Fig. 5(b) is the BEI for as-cast alloy#13 (Ag–55.0 at%Sb–40.0 at%Te). Although the primary phase is also the δ phase, the rest of the liquid moves toward the δ/$AgSbTe_2$ univariant line and the ternary $AgSbTe_2$ is solidified as second phase.

3.5. Primary phase: Sb

Fig. 6(a) is the BEI micrograph of alloy#15 (Ag–50.0 at%Sb–25.0 at%Te). The dendritic phase is the primary solidification phase. Its composition is Ag–99.3 at%Sb, and it is a Sb phase with very small amounts of Ag and Te solubilities. Similar results are found for alloy#16 and #17, as shown in Fig. 6(b) and (c), and all the primary solidification phase is the Sb phase. In addition to the Sb phase, the Ag_2Te phase with a composition of Ag–1.4 at%Sb–33.3 at%Te can be observed in Fig. 6(a)–(c). For all three alloys, the Ag_2Te phase is the secondary solidification phase. The δ phase is also found in the as-cast alloys. The existence of the δ phase indicates that the descending direction of the temperature

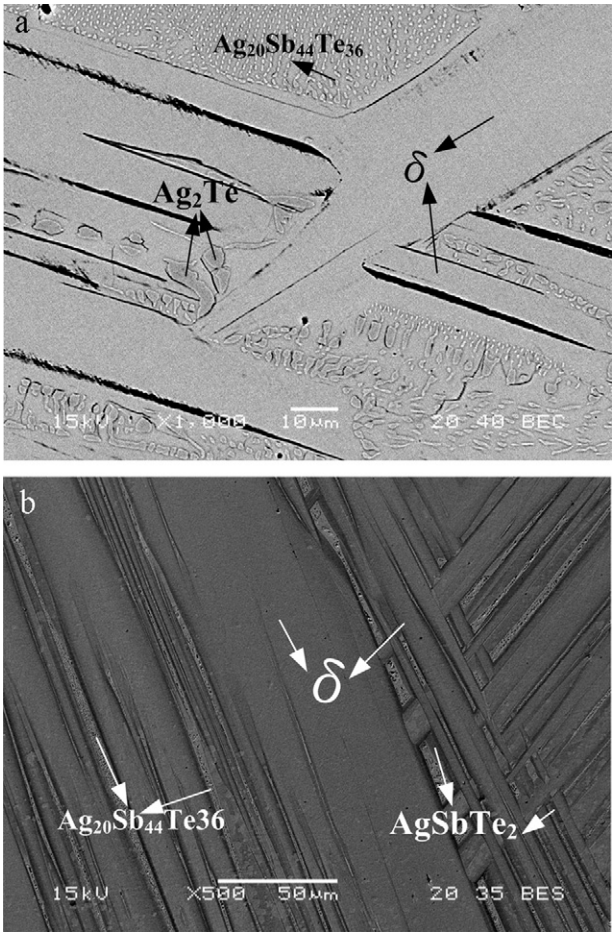

Fig. 5. (a) BEI micrograph of as-solidified alloy#14 (Ag–60.0 at%Sb–30.0 at%Te). (b) BEI micrograph of as-solidified alloy#13 (Ag–55.0 at%Sb–40.0 at%Te).

of the Sb/γ-Ag_2Te univariant line moves toward the δ phase direction.

3.6. Primary phase: ε, ξ, and Ag

Fig. 7(a) is the BEI micrograph of as-cast alloy#18 (Ag–3.0 at%Sb–7.0 at%Te). The dark dendritic phase is the primary phase and it is an Ag phase with a composition of 97.3 at%Ag. The rest of the matrix is primarily the secondary solidification phase, Ag_2Te. The results suggest that with the precipitation of the Ag phase, the liquid phase moves toward the Ag/γ-Ag_2Te univariant line. Fig. 7(b) is the BEI micrograph of as-cast alloy#19 (Ag–5.0 at%Sb–5.0 at%Te). Similar to that of alloy#18, the primary solidification phase is also the dendritic Ag phase. However, the secondary phase surrounding the Ag phase is the gray ξ phase. Different from that of alloy#18, the liquid phase moves toward the Ag/ξ univariant line with the solidification of the Ag phase. Fig. 7(c) is the BEI micrograph of as-cast alloy#20 (Ag–10.0 at%Sb–5.0 at%Te). The results are similar to those of alloy#19. The primary phase is the dendritic Ag phase, and the secondary phase is the ξ phase. Compared to that of alloy#19, alloy#20 has a larger amount of the ξ phase.

According to the binary Ag–Sb diagram [17], there are four different primary solidification phases, i.e. Sb, ε, ξ, and Ag, along the Ag–Sb side. Alloy#31 (Ag–30.0 at%Sb–5.0 at%Te) was initially presumed to be in the primary ε phase region but the microstructural examination results show that it is in the γ-Ag_2Te phase region. This result will be discussed later. This suggests that the liquidus

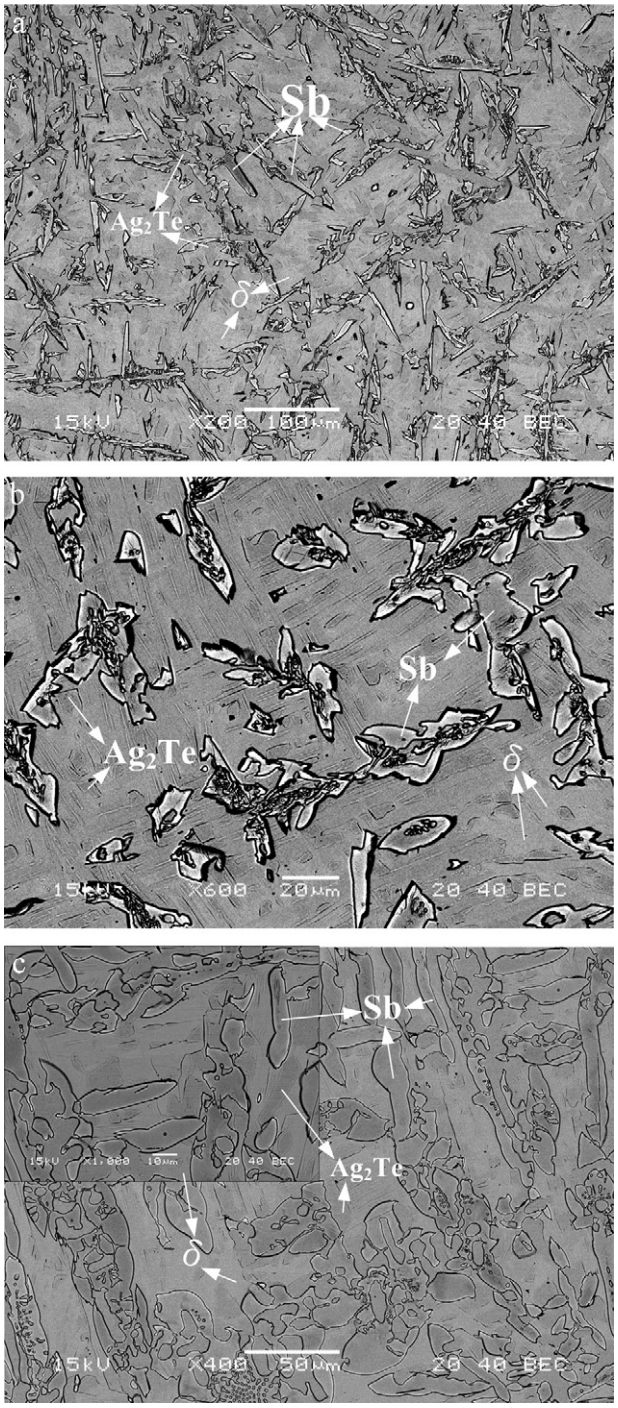

Fig. 6. (a) BEI micrograph of as-solidified alloy#15 (Ag–50.0 at%Sb–25.0 at%Te). (b) BEI micrograph of as-solidified alloy#16 (Ag–60.0 at%Sb–25.0 at%Te). (c) BEI micrograph of as-solidified alloy#17 (Ag–60.0 at%Sb–20.0 at%Te).

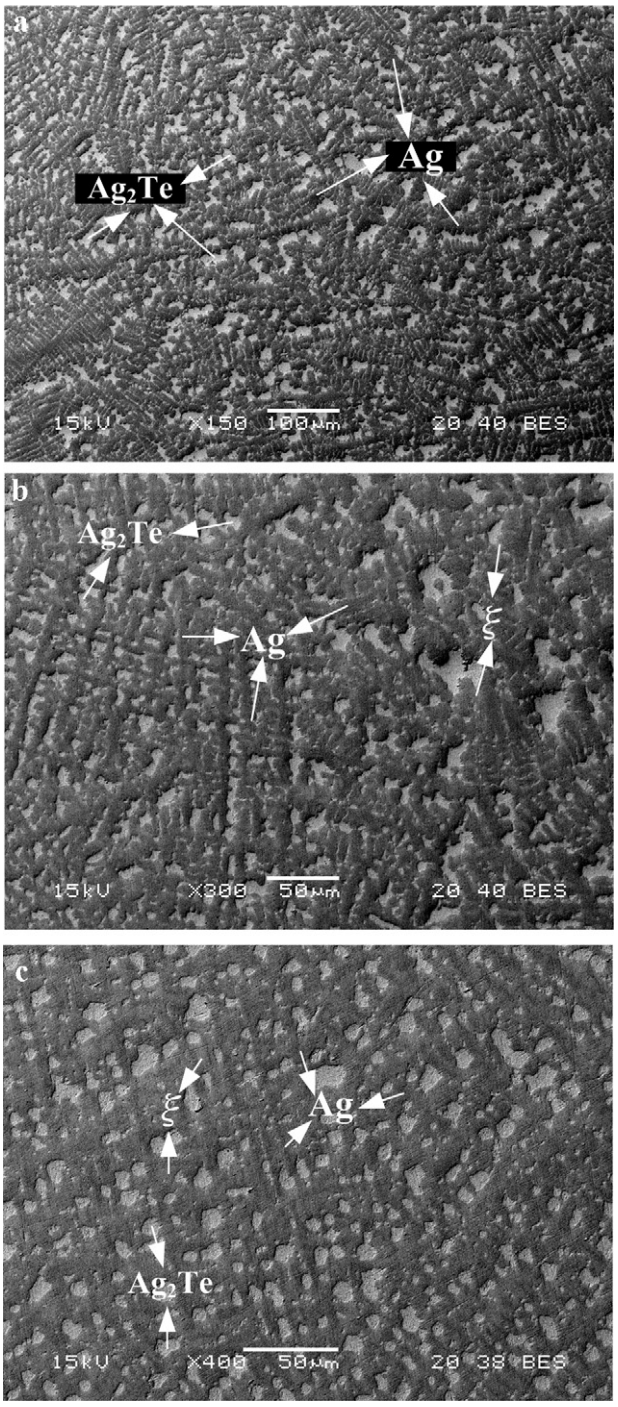

Fig. 7. (a) BEI micrograph of as-solidified alloy#18 (Ag–3.0 at%Sb–7.0 at%Te). (b) BEI micrograph of as-solidified alloy#19 (Ag–5.0 at%Sb–5.0 at%Te). (c) BEI micrograph of as-solidified alloy#20 (Ag–10.0 at%Sb–5.0 at%Te).

trough of γ-Ag_2Te/ε is close to the Ag–Sb side, as shown in Fig. 1(a) and (b).

3.7. Primary phase: γ-Ag_2Te, ß-Ag_2Te

Fig. 8(a) is the BEI micrograph of alloy#25 (Ag–40.0 at%Sb–30.0 at%Te). Three different phase regions are observed, including the dendritic phase, the brighter phase adjacent to the dendritic phase, and a fine microstructure region. The dendritic phase is the primary solidification phase. Its composition is Ag–1.9 at%Sb–33.8 at%Te, and it is an Ag_2Te phase. The composition of the brighter phase is Ag–53.8 at%Sb–34.9 at%Te, and it is a δ phase with the 11.4 at% solubility of Ag. Similar results are observed for alloy#27 (Ag–50.0 at%Sb–30.0 at%Te). The primary solidification phase is the dendritic Ag_2Te phase, and the secondary phase is the δ phase.

Fig. 8(b) is the BEI micrograph of alloy#32 (Ag–10.0 at%Sb–35.0 at%Te). Although the primary solidification phase is Ag_2Te phase as well, different from alloy#25, the secondary solidification phase is $AgSbTe_2$ [6,9] with the average composition of Ag–30.0 at%Sb–50.0 at%Te. In addi-

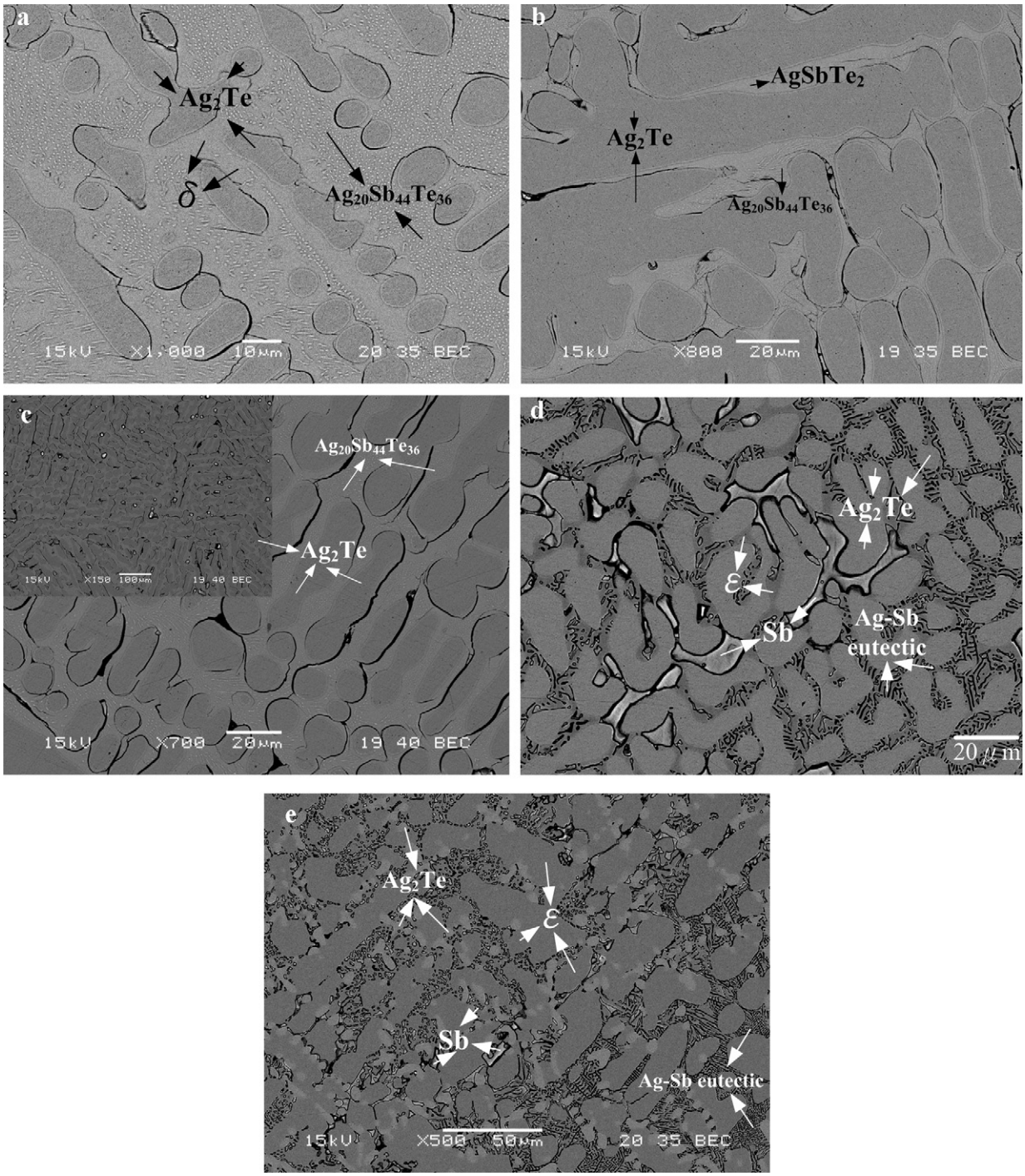

Fig. 8. (a) BEI micrograph of as-solidified alloy#25 (Ag–40.0 at%Sb–30.0 at%Te). (b) BEI micrograph of as-solidified alloy#32 (Ag–10.0 at%Sb–35.0 at%Te). (c) BEI micrograph of as-solidified alloy#29 (Ag–20.0 at%Sb–35.0 at%Te). (d) BEI micrograph of as-solidified alloy#30 (Ag–20.0 at%Sb–20.0 at%Te). (e) BEI micrograph of as-solidified alloy#31 (Ag–30.0 at%Sb–5.0 at%Te).

tion to the Ag_2Te and $AgSbTe_2$ phases, a fine microstructure region is also observed. Similar results are found for alloy#21 (Ag–30.0 at%Sb–40.0 at%Te), alloy#23 (Ag–35.0 at%Sb–38.0 at%Te) and alloy#28 (Ag–20.0 at%Sb–40.0 at%Te).

Fig. 8(c) is the BEI micrograph of alloy#29 (Ag–20.0 at%Sb–35.0 at%Te). Except for the primary solidification Ag_2Te phase, only a fine microstructure region is observed. Similar results are found for alloy#22 (Ag–30.0 at%Sb–36.0 at%Te). It is likely that the solidification paths of alloy#29 and #22 move directly toward the class I reaction, liquid = $\delta + Ag_2Te + AgSbTe_2$, with almost no interception of the univariant lines. Thus, only the primary solidification phase and a fine microstructural region are observed.

Fig. 8(d) is the BEI micrograph for as-cast alloy#30 (Ag–20.0 at%Sb–20.0 at%Te). Large quantities of bright phase are observed, which represent Ag_2Te phase with small Sb solubility. The Sb phase is adjacent to the primary Ag_2Te, which indicates the liquid moves toward the γ-Ag_2Te/Sb univariant line. The ε and the eutectic region in the matrix confirm that the solidification direction moves toward the Ag–Sb side and finally ends in the ternary or at the binary eutectic point. Fig. 8(e) shows the BEI micrographs for as-cast alloy#31 (Ag–30.0 at%Sb–5.0 at%Te),

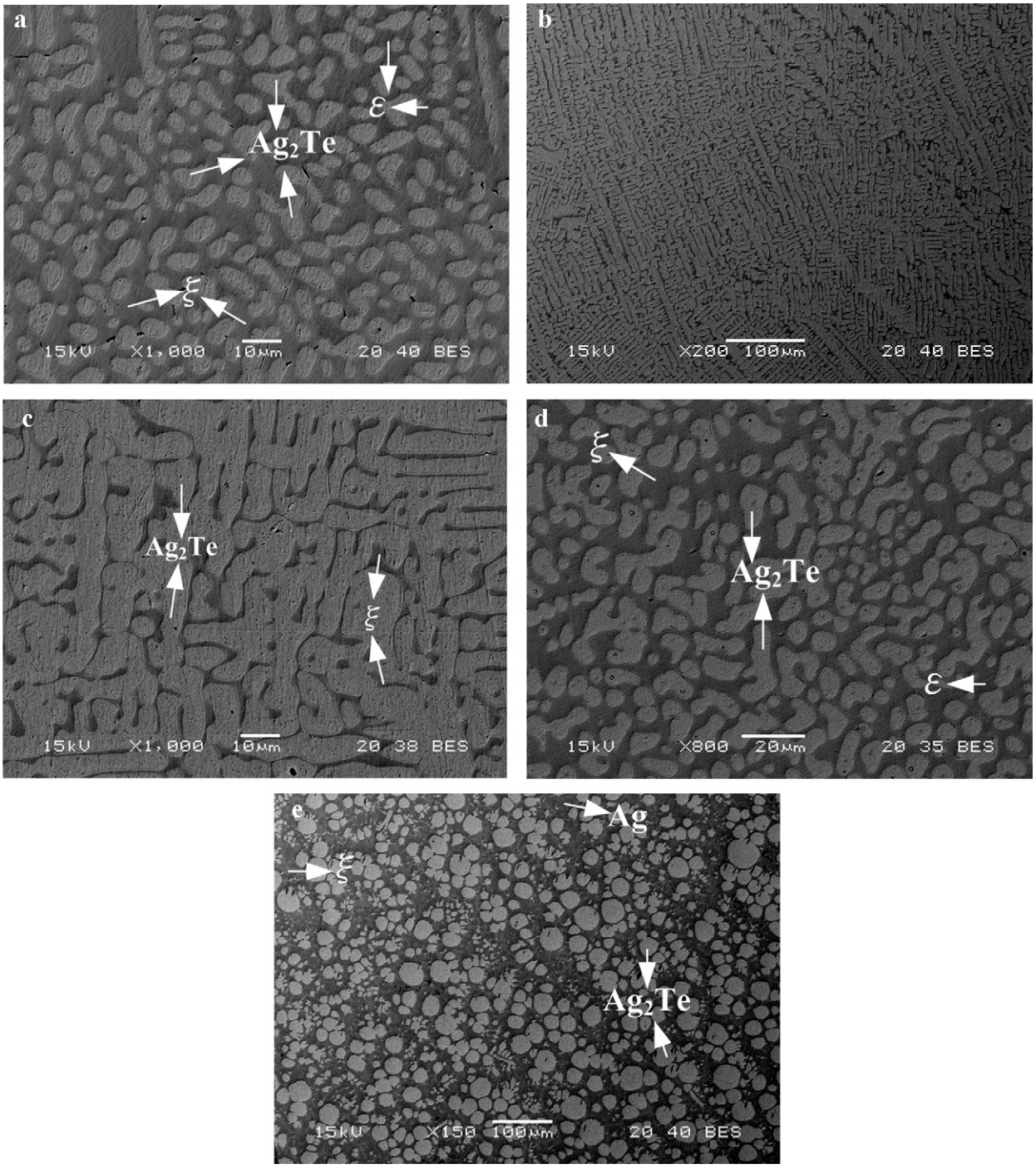

Fig. 9. (a) BEI micrograph of as-solidified alloy#33 (Ag–13.0 at%Sb–12.0 at%Te). BEI micrograph of as-solidified alloy#34 (Ag–5.0 at%Sb–25.0 at%Te) in (b) smaller magnifications, (c) larger magnifications. (d) BEI micrograph of as-solidified alloy#35 (Ag–8.0 at%Sb–15.0 at%Te). (e) BEI micrograph of as-solidified alloy#36 (Ag–5.0 at%Sb–13.0 at%Te).

and the microstructure is similar with alloy#30, except that the primary Ag_2Te is relatively small in amount and great quantities of ε phase are formed as the secondary phase.

Fig. 9(a) is the BEI micrograph of alloy#33 (Ag–13.0 at%Sb–12.0 at%Te). An interesting microstructure is observed and the bright spherical phases are uniformly dispersed in the matrix. The microstructure indicates the existence of a liquid miscibility gap which extends from the Ag–Te binary edge [16,21,22]. An enlarged liquidus projection at the Ag-rich corner is shown in Fig. 10. Alloy#33 was inside the miscibility gap at 1000 °C, and there were two liquids, L_1 and L_2. During the cooling process, the relatively Ag-rich L_1 phase region moves toward the primary ξ regime, while the relatively Te-rich L_2 phase moves toward the primary Ag_2Te regime. It should be mentioned that the critical point of the liquidus miscibility gap is drawn without experimental proof and needs to be verified in a future study.

Fig. 9(b) and (c) are the BEI micrographs of alloy#34 (Ag–5.0 at%Sb–25.0 at%Te) with smaller and larger magnification rates. The nominal composition of alloy#34 is close to the boundary of the miscibility dome. A larger amount of bright phase which solidified from L_2 is surrounded by darker phase. The average composition of the bright phase is Ag–5.7 at%Sb–27.1 at%Te, similar to that in the as-solidified L_2 in alloy#33. The dark phases are composed of the ξ and ε phases with compositions of Ag–16.2 at%Sb

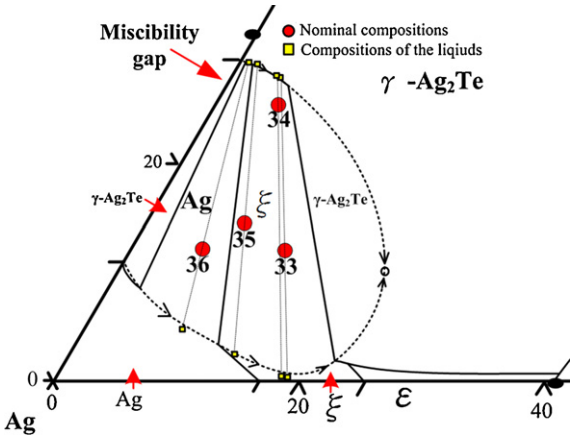

Fig. 10. Enlargement of the Ag–Sb–Te liquidus projection at the Ag-rich corner superimposed with the alloys examined in this study.

and Ag–21.0 at%Sb, respectively. Both of the two Ag–Sb compounds contain negligible Te-solubility. Similar results can be found in the as-solidified alloy#35 (Ag–8.0 at%Sb–15.0 at%Te), and alloy#36 (Ag–5.0 at%Sb–13.0 at%Te), as shown in Fig. 9(d) and (e), respectively.

Fig. 11(a) and (b) are the BEI micrographs of alloy#37 (Ag–5.0 at%Sb–45.0 at%Te) and alloy#38 (Ag–3.0 at%Sb–45.0 at%Te). The darker dendritic phase is the primary phase and the compositional analysis results indicate

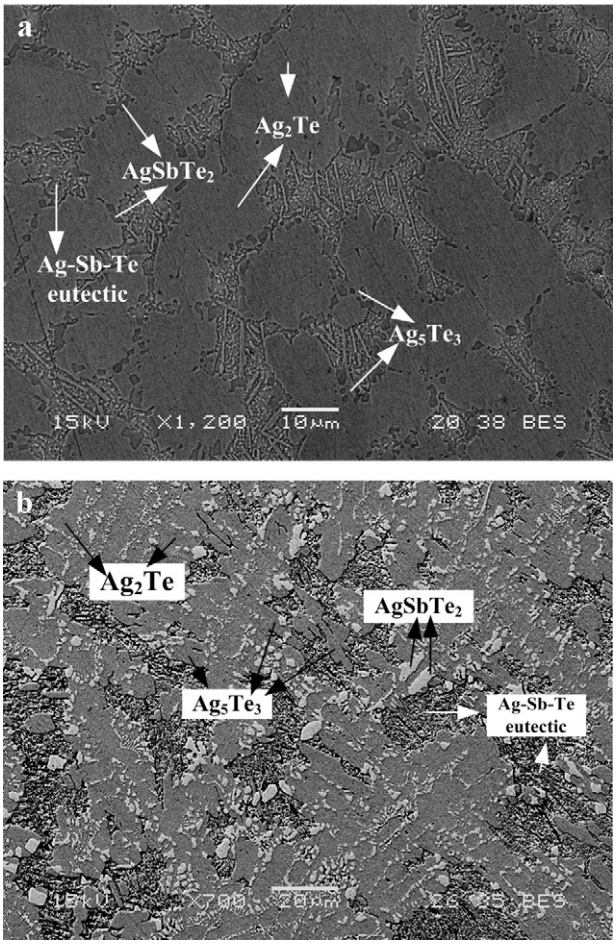

Fig. 11. (a) BEI micrograph of as-solidified alloy#37 (Ag–5.0 at%Sb–45.0 at%Te). (b) BEI micrograph of as-solidified alloy#38 (Ag–3.0 at%Sb–45.0 at%Te).

they are in the Ag_2Te phase. According to the binary Ag–Te phase diagram [16], the γ-Ag_2Te transforms to ß-Ag_2Te at lower temperatures, and alloy#37 and #38 are close to the ß-Ag_2Te primary phase region. However, no distinction could be made in this study between the γ-Ag_2Te and ß-Ag_2Te. A dashed line is drawn arbitrarily between the γ-Ag_2Te/ß-Ag_2Te as a reminder of the possible existence of this boundary without proof. Small amounts of the ternary $AgSbTe_2$ phase are also found in as-solidified alloy#37 and #38, and the fine structure region is a mixture phase region.

3.8. Primary phase: ß-$Ag_{1.9}Te$ and ß-Ag_5Te_3

Fig. 12(a) is the BEI micrograph of alloy#39 (Ag–5.0 at%Sb–52.0 at%Te). The micrograph on the upper-left corner is a micrograph with a smaller magnification rate. There are at least three different phase regions, the relatively large twig-like phase, a dark phase adjacent to the twig-like phase, and a multi-phase mixture region. Based on the microstructure, the twig-like phase is the primary solidification phase. Its composition is Ag–1.7 at%Sb–38.1 at%Te, and it is a ß-Ag_5Te_3 phase with 1.7 at% solubility of Sb. According to the binary Ag–Te phase diagram [16], there are two different primary solidification phases around this compositional regime, ß-$Ag_{1.9}Te$ and ß-Ag_5Te_3. It should be mentioned that these two phases are very similar and no distinction between them could be made in this study. Moreover the ß-Ag_5Te_3 phase identified here could be the ß-$Ag_{1.9}Te$ phase.

The composition of the darker and smaller phase adjacent to the ß-Ag_5Te_3 phase is Ag–30.1 at%Sb–48.8 at%Te, and it is a ternary $AgSbTe_2$ phase. As shown in Fig. 1(b), the liquid composition moves toward the ß-Ag_5Te_3 + $AgSbTe_2$ univariant line with the precipitation of the ß-Ag_5Te_3 phase, and the $AgSbTe_2$ phase is the secondary solidification phase. The illustration is in agreement with the observation that the $AgSbTe_2$ phase is adjacent to the primary ß-Ag_5Te_3 phase. The majority of this sample is a multi-phase mixture region. It is likely the final solidification part occurs through the class I reaction, liquid = ß-Ag_5Te_3 + $AgSbTe_2$ + Te. Similar results are observed for alloy#40 (Ag–5.0 at%Sb–56.0 at%Te) and #41 (Ag–5.0 at%Sb–60.0 at%Te) as shown in Fig. 12(b) and (c), respectively. Since this study does not differentiate the ß-$Ag_{1.9}Te$ and ß-Ag_5Te_3 phases, the ß-$Ag_{1.9}Te$/ß-Ag_5Te_3 univariant line is drawn as a dashed line.

3.9. Primary phase: $AgSbTe_2$

Fig. 13(a) is the BEI micrograph of as-cast alloy#44 (Ag–10.0 at%Sb–52.0 at%Te). The composition of the dendritic phase is Ag–20.6 at%Sb–50.4 at%Te and it is a ternary $AgSbTe_2$ phase. This has been reported in previous studies and it considered as a remarkable thermoelectric material [6–9]. A brighter phase is formed adjacent to the $AgSbTe_2$ phase. Its composition is Ag–3.0 at%Sb–37.5 at%Te and it is ß-Ag_5Te_3 phase. Similar results are found for as-cast alloy#42 (Ag–10.0 at%Sb–60.0 at%Te), alloy#47 (Ag–20.0 at%Sb–52.0 at%Te), alloy#48 (Ag–20.0 at%Sb–45.0 at%Te), alloy#49 (Ag–30.0 at%Sb–50.0 at%Te), alloy#50 (Ag–35.0 at%Sb–45.0 at%Te), alloy#51 (Ag–40.0 at%Sb–40.0 at%Te), and the primary phase of all of the above alloys is ternary $AgSbTe_2$.

Fig. 13(b) is the BEI micrograph of alloy#45 (Ag–10.0 at%Sb–45.0 at%Te). In addition to the primary $AgSbTe_2$ phase, the eutectic type lamellar microstructures of $AgSbTe_2$ and Ag_2Te are observed. It has been proposed that there is a pseudo binary eutectic reaction, L = $AgSbTe_2$ + Ag_2Te [6], at 70 at%Ag_2Te in the Ag_2Te–Sb_2Te_3 system at 544 °C. Based on the metallographic observation, it is very likely that the lamellar structure of alloy#45 was formed through this eutectic reaction. To further confirm the existence of this pseudo binary eutectic reaction, alloy#46 was prepared with this eutectic composition

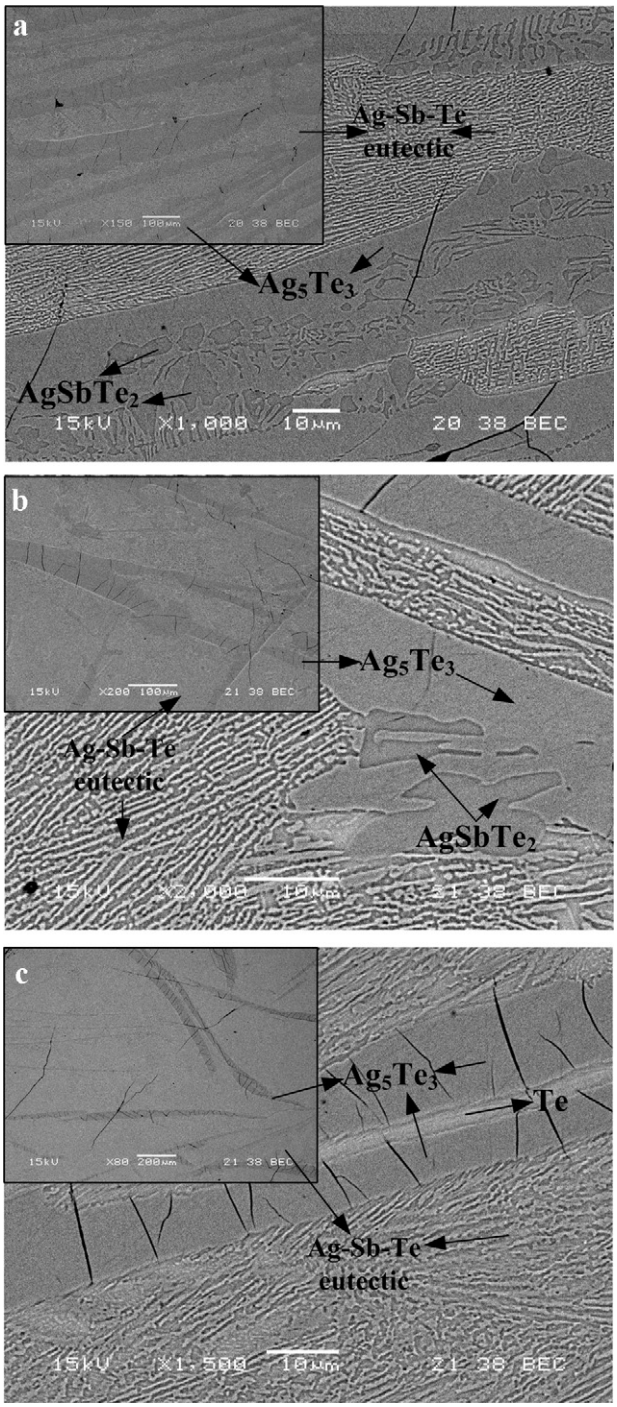

Fig. 12. (a) BEI micrograph of as-solidified alloy#39 (Ag–5.0 at%Sb–52.0 at%Te). (b) BEI micrograph of as-solidified alloy#40 (Ag–5.0 at%Sb–56.0 at%Te). (c) BEI micrograph of as-solidified alloy#41 (Ag–5.0 at%Sb–60.0 at%Te).

(Ag–15.0 at%Sb–45.0 at%Te). Fig. 13(c) is the BEI micrograph of the as-cast alloy#46 (Ag–15.0 at%Sb–45.0 at%Te). Similar to the microstructure of alloy#44, a lamellar structure of $AgSbTe_2$ and Ag_2Te is formed. The brighter phase is confirmed to be Ag_2Te and the darker phase is $AgSbTe_2$.

It has been reported that the microstructures are very important to the thermoelectric properties [10–12]. Self-assembled nanometer lamellae of PbTe and Sb_2Te_3 was prepared using the rapid solidification method [23], and it was found that the thermoelectric properties were improved with randomly distributed phases with feature sizes in nanometer to sub-micrometer. As shown in Fig. 13(b) and (c), a lamellar structure of $AgSbTe_2$ and Ag_2Te phases was produced with normal quenching. The orientation of the lamellae seems randomly distributed in different grains. The spacing of lamellae, less than 1 μm, is quite uniform.

Fig. 13(d) is the BEI micrograph of alloy#51 (Ag–40.0 at%Sb–40.0 at%Te). In addition to the primary $AgSbTe_2$ solidification phase, there are regions with very fine microstructures. The sizes of the tiny bright particulates in the fine structure region are around 200–400 nm, and it is difficult to determine the composition quantitatively. According to the liquidus projection, the fine microstructure region is the final solidified ternary eutectic. Fine microstructure regions have been observed and mentioned previously various alloys, such as alloys#10–#13, #21–#23 and #25–#27, etc.

3.10. Class I, liquid = δ + Ag_2Te + $AgSbTe_2$

Fig. 14(a) and (b) are the BEI micrographs of alloy#24 (Ag–40.0 at%Sb–36.0 at%Te). Very fine microstructure is observed. The average composition of the fine microstructure region is homogenous. No primary solidification phase can be observed, as shown in Fig. 14(a), which shows a lower magnification rate. The XRD results show three phases, $AgSbTe_2$, Ag_2Te and δ, as shown in Fig. 14(c). The results are in agreement with the proposed liquidus projection which determined that alloy#24 is at class I reaction composition. A closer look of the microstructure in larger magnification, as shown in Fig. 14(b), reveals that the white precipitates are in sub-micrometer size and are aligned in specific directions in different grains.

The size of the bright phase is about 200–400 nm, as shown Fig. 14(d), which shows the secondary electron image (SEI) of the specimen taken from the quenched alloy#24 by using the focused ion beam (FIB) technique. Color-mapping technique is carried out by field-emission EPMA with a magnification of 6000×, and the results are shown in Fig. 14(e). The bright particulate is in the Ag-rich phase, which is the Ag_2Te phase.

Fig. 13(d) is the BEI micrograph of alloy#51 solidified after air-cooling. In addition to the $AgSbTe_2$ and δ phases, regions of fine microstructure with the bright Ag_2Te phase are observed. Alloy#51 is compositionally near the $AgSbTe_2$/δ univariant line. After the solidification of the primary $AgSbTe_2$ and the secondary δ phase, the residual liquid then passes through the class I reaction point and forms fine microstructure in the matrix.

It is worth of mentioning that the materials with fine and uniform microstructure are less brittle, which is a common problem of Te-bearing materials. Furthermore, thermoelectric alloys with sub-micrometer sized microstructure are reported with exceptionally excellent thermoelectric efficiency [10–12,23]. Alloy#24 is likely a good candidate to be a good thermoelectric material; this alloy could easily be prepared simply through water-quenching of the melt.

3.11. Thermal analysis results

The phase transformation temperatures are determined by thermal analysis. Since superheating effect is usually not as significant [24–27], the temperatures reported in this study are thus determined from the heating curves of DTA. The determinations of temperatures from the heating curves are based on the theory described previously [24–27]. It should be noted that the DTA heating and cooling curves shown in Fig. 15(a)–(c) are based on raw data without calibration. A calibration curve is constructed based on the DTA results of pure Sn, In, Zn, Pb and Sb. The phase transformation temperatures reported in the text for alloys#1, #11, #24, #30, #37, #47, #49 and #51 are all calibrated results. These results are summarized in Table 2.

Fig. 15(a) shows the DTA heating and cooling curves of alloy#24 (Ag–40.0 at%Sb–36.0 at%Te). Based on the metallographic observation, the alloy is at the ternary eutectic point. Only one reaction peak can be found in the DTA heating curve of alloy#24, at 496.5 °C. This is in agreement with the proposed class I reaction: liquid = δ + Ag_2Te + $AgSbTe_2$. It is worthy of mentioning that the difference between the onset temperatures of the cooling and heating curves as shown in Fig. 15(a) is small, and it is an indication that the undercooling is not significant for the solidification of this alloy. In some situations and some alloys, undercooling is large and it could change the solidified microstructures and even alter the sequence of solidification phases [28]. The undercooling effect thus brings experimental uncertainties in the determination of primary solidification phase, and could possibly be the reason for the dash lines as shown in Fig. 1(a) and (b).

Fig. 15(b) is the DTA heating and cooling curve of alloy#1 (Ag–5.0 at%Sb–70.0 at%Te). Three reaction peaks are observed. The peak with the lowest temperature, at 323.9 °C, results from the class I reaction: L = β-Ag_5Te_3 + $AgSbTe_2$ + Te. The second peak, at 380.4 °C, is from the L = Te + β-Ag_5Te_3 univariant reaction. The peak at 408.7 °C is relatively small and broad and is the liquidus temperature. The thermal analysis results are consistent with the

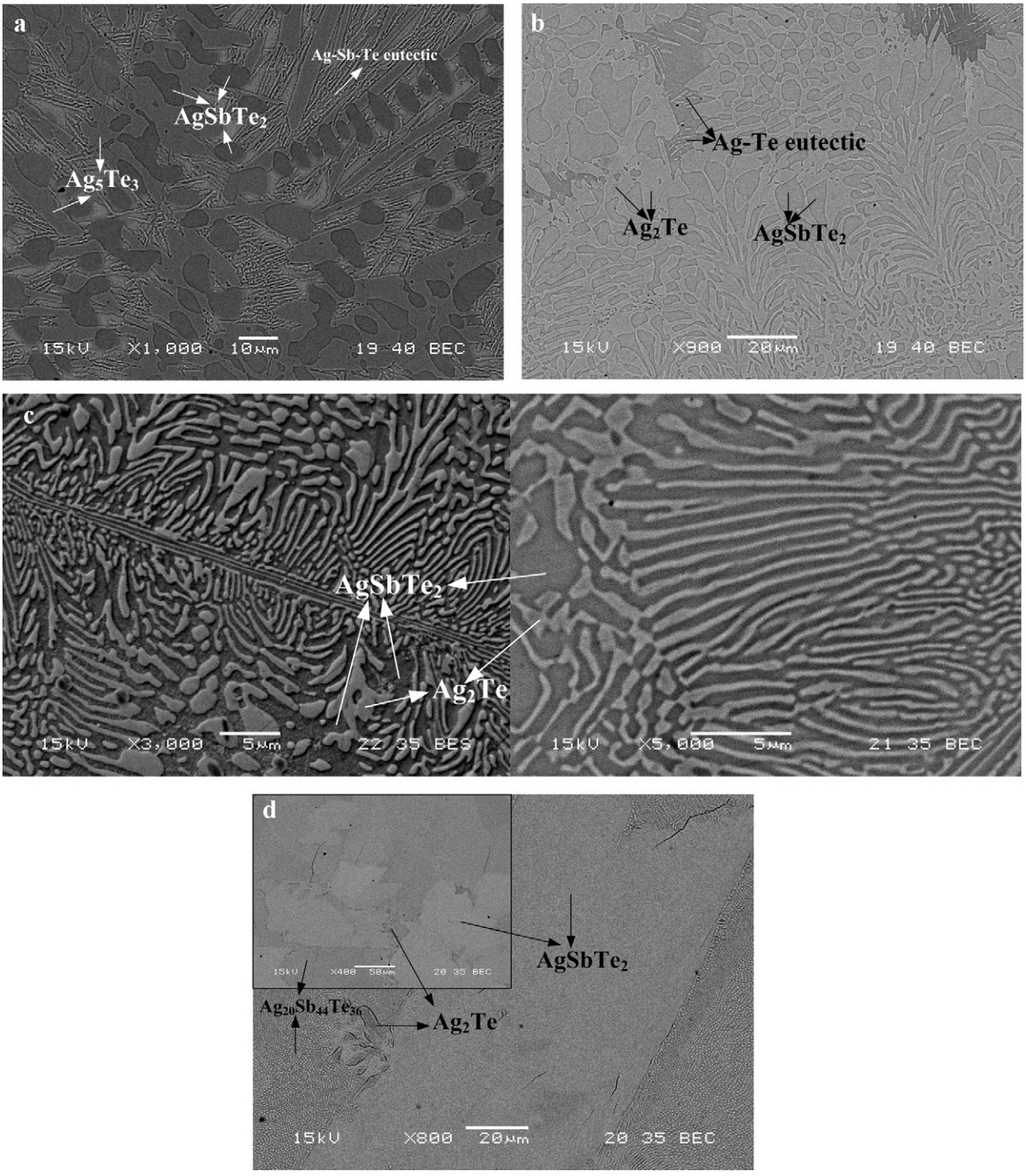

Fig. 13. (a) BEI micrograph of as-solidified alloy#44 (Ag–10.0 at%Sb–52.0 at%Te). (b) BEI micrograph of as-solidified alloy#45 (Ag–10.0 at%Sb–45.0 at%Te). (c) BEI micrograph of as-solidified alloy#46 (Ag–15.0 at%Sb–45.0 at%Te). (d) BEI micrograph of as-solidified alloy#51 (Ag–40.0 at%Sb–40.0 at%Te).

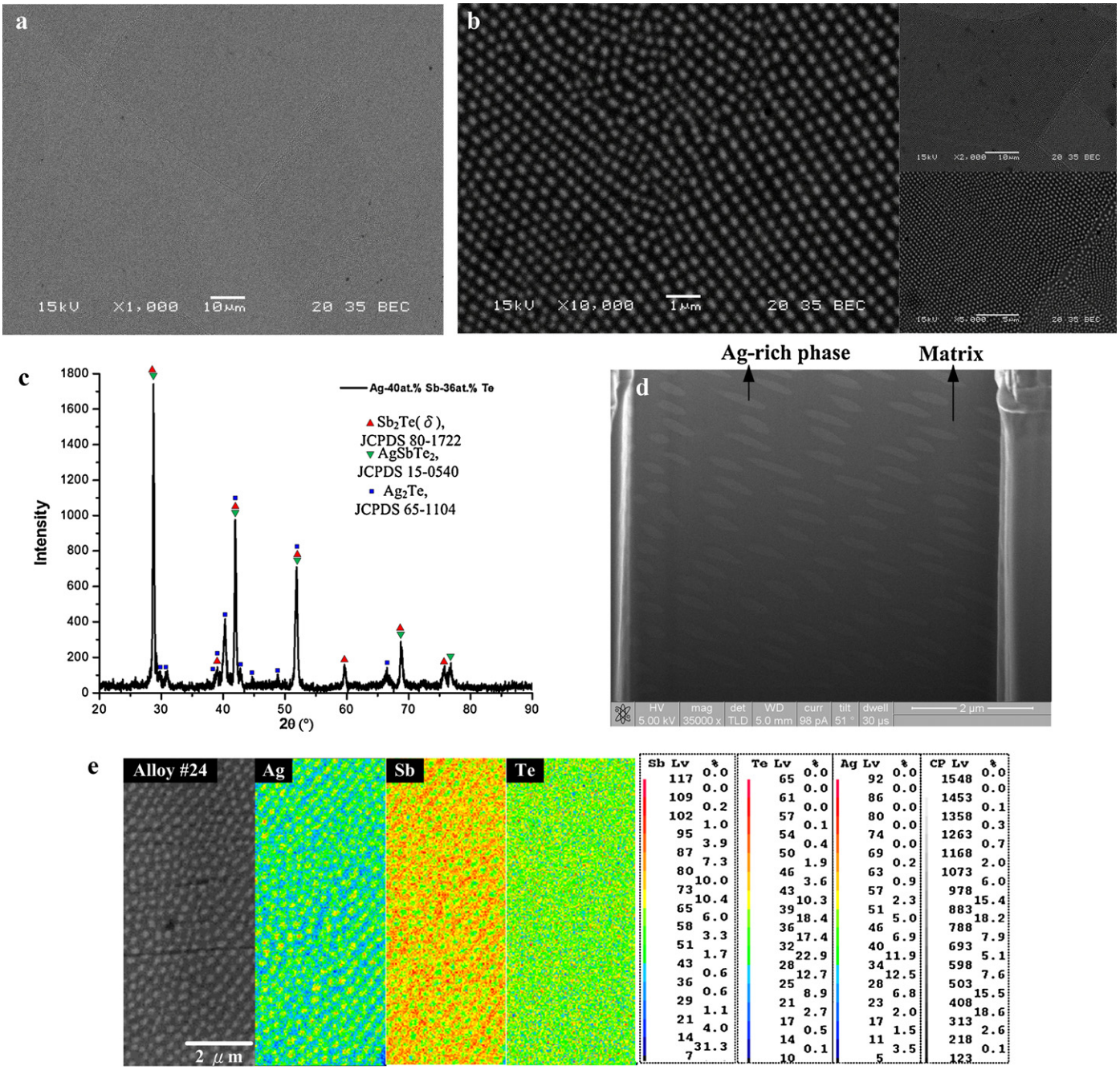

Fig. 14. BEI micrograph of alloy#24 (Ag–40.0 at%Sb–36.0 at%Te) solidified by water-quenching in (a) smaller magnifications, (b) larger magnifications. (c) X-ray diffraction pattern of as-solidified alloy#24 (Ag–40.0 at%Sb–36.0 at%Te). (d) SEI micrograph of alloy#24 (Ag–40.0 at%Sb–36.0 at%Te) obtained by focused ion beam (FIB) in the perpendicular direction, the feature size of bright circular phase is around 200–400 nm. (e) Color-mapping results of alloy#24 (Ag–40.0 at%Sb–36.0 at%Te) obtained by field-emission EPMA.

Table 2
Phase transformation temperatures determined by DTA heating curves of the ternary Ag–Sb–Te alloys.

No.	Nominal composition (at%)			Primary phase	Phase transition temperature (°C)			
	Ag	Sb	Te		1st	2nd	3rd	4th
1	25.0	5.0	70.0	Te	323.9	380.4	408.7	–
11	10.0	50.0	40.0	δ	495.1	502.9	505.3	–
24	24.0	40.0	36.0	–	496.5	–	–	–
30	60.0	20.0	20.0	γ-Ag_2Te	128.8	470.1	479.3	777.8
37	50.0	5.0	45.0	β-Ag_2Te	323.3	356.3	395.6	430.7
47	28.0	20.0	52.0	$AgSbTe_2$	324.1	358.7	543.7	–
49	20.0	30.0	50.0	$AgSbTe_2$	555.1	–	–	–
51	20.0	40.0	40.0	$AgSbTe_2$	496.4	501.6	–	–

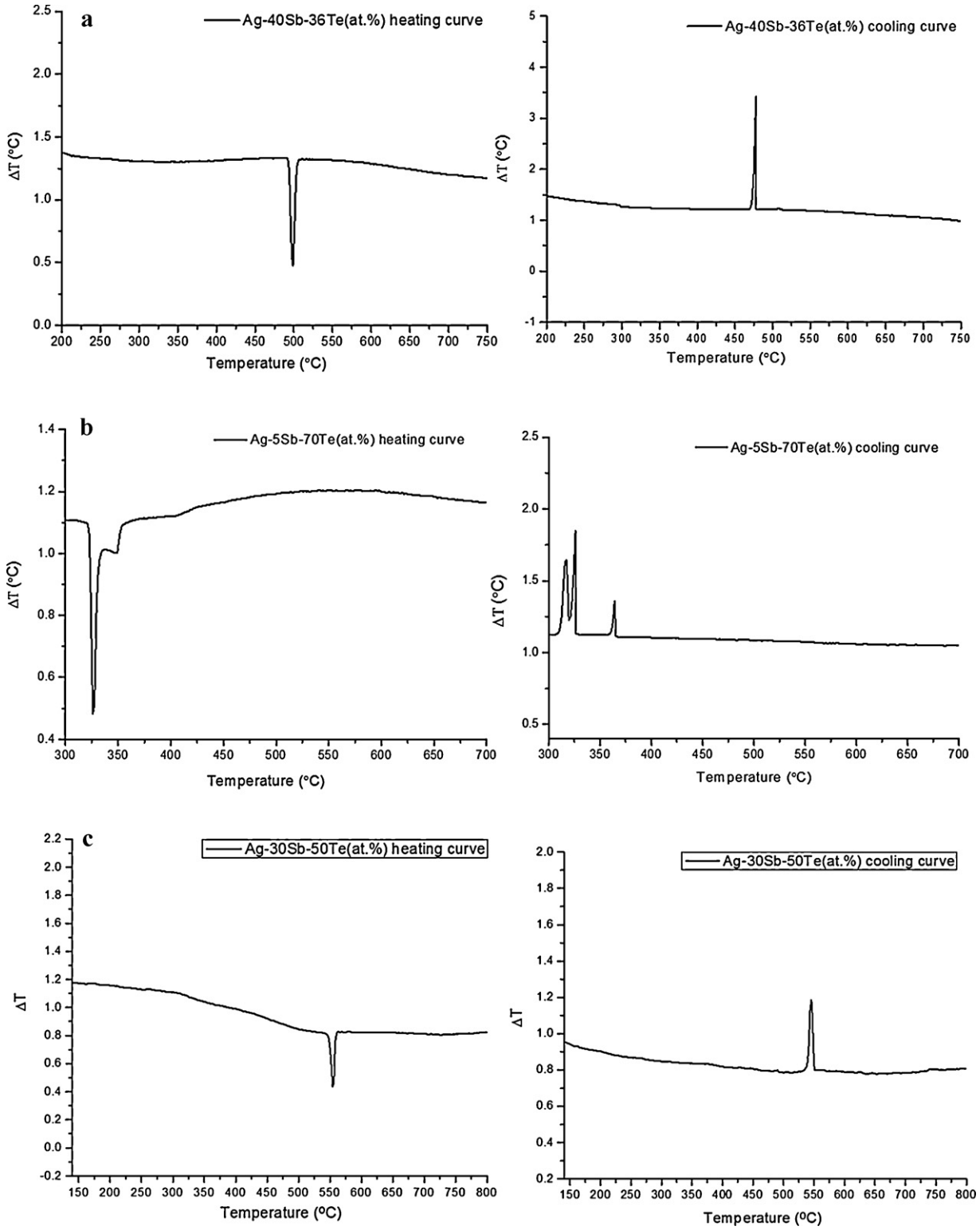

Fig. 15. DTA heating and cooling curves of (a) alloy#24 (Ag–40.0 at%Sb–36.0 at%Te), (b) alloy#1 (Ag–5.0 at%Sb–70.0 at%Te), (c) alloy#49 (Ag–30.0 at%Sb–50.0 at%Te).

metallographic observation mentioned above. Fig. 15(c) is the DTA heating and cooling curve for alloy#49 (Ag–30.0 at%Sb–50.0 at%Te) with nominal composition of the ternary $AgSbTe_2$ phase. The melting point of this ternary compound has been determined previously [29,30]. This study determined the melting point temperature to be 555.1 °C, which is in good agreement with the findings of Wernick and Benson [29].

4. Conclusions

Thirteen primary solidification phase regions, including a ternary $AgSbTe_2$ phase region, are found in the ternary Ag–Sb–Te system. The Ag–Sb–Te liquidus projection is proposed based on metallographic observations and the thermal analysis results of the ternary alloys, and the phase equilibrium information

of three constituent binary systems. Very fine microstructures with Ag_2Te phase feature sizes in nanometers are observed. These microstructures are resulted from the class I reaction, liquid = $\delta + Ag_2Te + AgSbTe_2$, with the liquid composition of Ag–40.0 at%Sb–36.0 at%Te at 496.5 °C. Since it has been reported that bulk thermoelectric materials with dispersed phase could have very good thermoelectric properties, alloys with nano-size Ag_2Te ought to be investigated further. In addition, a unique microstructure with bright spherical phases uniformly dispersed in a matrix is found, and is resulted from a liquid miscibility gap extending from the Ag–Te binary edge into the ternary system at the Ag-rich corner.

Acknowledgement

The authors acknowledge the financial support of National Science Council in Taiwan through grant #NSC97-2221-E-007-067-MY3.

References

[1] F.R. Yu, J.J. Zhang, D.L. Yu, J.L. He, Z.Y. Liu, Bo Xu, Y.J. Tian, J. Appl. Phys. 104 (2009) 094303–094305.
[2] B.A. Cook, M.J. Kramer, J.L. Harringa, M.K. Han, D.Y. Chung, M.G. Kanatzidis, Adv. Mater. 19 (2009) 1254–1259.
[3] K.F. Hsu, S. Loo, F. Guo, W. Chen, J.S. Dyck, C. Uher, T. Hogan, E.K. Polychroniadis, M.G. Kanatzidis, Science 303 (2004) 818–821.
[4] J. Androulakis, K.F. Hsu, R. Pcionek, H. Kong, C. Uher, J.J. D'Angelo, A. Downey, T. Hogan, M.G. Kanatzidis, Adv. Mater. 18 (2006) 1170–1173.
[5] B. Poudel, Q. Hao, Y. Ma, Y. Lan, A. Minnich, B. Yu, X. Yan, D. Wang, A. Muto, D. Vashaee, X. Chen, J. Liu, M.S. Dresselhaus, G. Chen, Z. Ren, Science 320 (2008) 634–638.
[6] M.R. Marie, G. Brun, J.C. Tedenac, J. Mater. Sci. 20 (2) (1985) 730–735.
[7] B.A. Cook, X. Wei, J.L. Harringa, M.J. Kramer, J. Mater. Sci. 42 (2007) 7643–7646.
[8] S.H. Yang, T.J. Zhu, T. Sun, J. He, S.N. Zhang, X.B. Zhao, Nanotechnology 19 (2008) 245707–245711.
[9] J.D. Sugar, D.L. Medlin, J. Alloys Compd. 478 (2009) 75–82.
[10] T. Ikeda, V.A. Ravi, G.J. Snyder, Acta Mater. 57 (2009) 666–672.
[11] T. Ikeda, V.A. Ravi, G.J. Snyder, Metall. Mater. Trans. A 41 (2010) 641–650.
[12] T. Ikeda, S.M. Haile, V.A. Ravi, H. Azizgolshani, F. Gascoin, G.J. Snyder, Acta Mater. 55 (2007) 1227–1239.
[13] F.N. Rhines, Phase Diagrams in Metallurgy, Their Development and Application, McGraw-Hill, New York, 1956.
[14] S.W. Chen, C.H. Wang, S.K. Lin, C.N. Chiu, C.C. Chen, JOM 59 (2007) 41–45.
[15] S.K. Lin, C.F. Yang, S.H. Wu, S.W. Chen, J. Electron. Mater. 37 (4) (2008) 498–506.
[16] I. Karakaya, W.T. Thompson, J. Phase Equilib. 12 (1991) 56–63.
[17] C.S. Oh, J.H. Shim, B.J. Lee, D.N. Lee, J. Alloys Compd. 238 (1996) 155–166.
[18] G. Ghosh, J. Phase Equilib. 15 (3) (1994) 349–360.
[19] M.C. Flemings, Solidification Processing, McGraw-Hill, New York, 1974.
[20] J.D. Verhoeven, Fundamentals of Physical Metallurgy, John Wiley & Sons, New York, 1975.
[21] L. Ratke, S. Diefenbach, Mater. Sci. Eng. RIS (1995) 263–347.
[22] D. Mirković, J. Grőbner, R. Schmid-Fetzer, Acta Mater. 56 (2008) 5214–5222.
[23] T. Ikeda, L.A. Collins, V.A. Ravi, F.S. Gascoin, S.M. Haile, G.J. Snyder, Chem. Mater. 19 (4) (2007) 763–767.
[24] S.W. Chen, C.C. Huang, J.C. Lin, Chem. Eng. Sci. 50 (3) (1995) 417–431.
[25] S.W. Chen, C.C. Huang, Acta Mater. 44 (1996) 1955–1965.
[26] S.C. Jeng, S.W. Chen, Acta Mater. 45 (1997) 4887–4899.
[27] W.J. Boettinger, U.R. Kattner, Metall. Mater. Trans. A 33A (2002) 1779–1794.
[28] Y.C. Huang, S.W. Chen, K.S. Wu, J. Electron. Mater. 39 (1) (2010) 109–114.
[29] J.H. Wernick, K.E. Benson, Phys. Soc. 3 (1957) 157–159.
[30] R.M. Ayral-Marin, G. Brun, M. Maurin, J.C. Tedenac, Eur. Solid State Inorg. Chem. 27 (5) (1990) 747–757.